Research Article

Pulsed Laser Cladding of NiCrBSiFeC Hardcoatings Using Single-Walled Carbon Nanotube Additives

Alexandru Pascu [iD],[1] **Elena Manuela Stanciu,**[1] **Catalin Croitoru** [iD],[1] **Ionut Claudiu Roată,**[1] **Julia Mirza Rosca,**[2] **Cimpoesu Nicanor,**[3] **Mircea Horia Ţierean,**[1] **and Cristina Bogatu**[4]

[1]*Faculty of Materials Science and Engineering, Transilvania University of Brasov, Brasov 50000, Romania*
[2]*Department of Mechanical Engineering, University of Las Palmas de Gran Canaria (ULPGC), Tafira, 35017 Canary Islands, Spain*
[3]*Faculty of Materials Science and Engineering, Tech Univ Gheorghe Asachi Iasi, Iasi 700050, Romania*
[4]*R&D Center Renewable Energy System and Recycling, Transilvania University of Brasov, Eroilor 29 Street, 500036 Brasov, Romania*

Correspondence should be addressed to Alexandru Pascu; alexandru.pascu@unitbv.ro

Carbonaceous nanoscale additives present a pronounced influence on the mechanical properties of both metallic and plastic materials. This paper addresses the fabrication of composite coatings by laser cladding of single-walled carbon nanotubes incorporated by ball milling into a nickel-based powder (NiCrBSiFeC). The coatings were obtained by using the preplaced laser cladding technique on steel substrates. Optical microscopy and SEM microscopy were used to characterise the microstructure refinement of the coatings, and the mechanical behaviour of the coatings has been studied through wear and micro-/nanohardness testing.

1. Introduction

The obtainment of durable metal coatings with improved mechanical strength, wear, and corrosion resistance represents both a milestone and a focal point of the research conducted in the last decades in the field of material development [1]. A necessary means to obtain performant coatings is represented by microstructural refinement, which can provide grain morphology and grain boundary control, as well as impede dislocation movement [2]. Microstructural refinement of metallic materials can be usually achieved through several methods ranging from thermal treatment, plastic deformation [3], and dispersion strengthening with oxide, carbide, and boride hard phases [4, 5] to microalloying [6].

Shifting the technological barriers in the field of metallic coatings to further levels, dictated by the need for "greener" and cost-effective technologies and for lighter metallic materials and by the overall increasing trend in the price of alloying elements and dispersion phases, has deter-mined a growing interest for embedding nanomaterials (with emphasis on carbon-derived nanomaterials) into the metal phase. The high aspect ratio of nanomaterials, coupled with their remarkable mechanical properties, chemical stability, and higher available surface area for interacting at the atomic level with the embedding host material, has led to the obtainment of materials with unique properties, not found otherwise when using ordinary micro- and macroscale materials [7–9].

Up to date, two types of nanomaterials have been employed for embedding in bulk metal phases, namely, ceramic nanoparticles (carbides, nitrides, borides, oxides, and metal sulphides) [7, 10, 11] and carbonaceous nano-structures, such as nanotubes (CNTs) [7, 9, 12–15] or graphene oxide [1, 2] with emphasis on the former type. Even if carbon nanotube reinforcement of polymer matrices has been studied in detail so far, relatively few research has been conducted regarding the application of these nanomaterials to improve the mechanical properties of metallic materials [2]. Generally, two distinct mechanisms are responsible for

this improvement, depending on the nature of the metal matrix: (1) the carbonaceous nanomaterials react with the metal phase in a molten state, generating carbides with high hardness [12, 16], or (2) they do not dissolve into the metal phase, providing, in turn, mechanical strengthening, either through load transfer effect, through refinement of metal grains (the CNTs are located at the grain boundaries), or through interaction with dislocations at the atomic level [7, 17]. The former mechanism was reported for titanium [12, 15], aluminium-copper alloys [18], and silicon-rich metal alloys [19], while the latter was reported, for example, in the case of mild steel [20], pure iron [21], nickel [14], aluminium [22, 23], magnesium [8], and copper [9, 24, 25]. When embedded in the metal, good interfacial adhesion between CNT and the metal phase has been observed, due to the formation of a thin intermediary layer of metal carbide on the nanomaterial surface, avoiding delamination [26].

While there are several studies focused on bulk material obtainment through powder metallurgy methods for metal-carbonaceous nanomaterial assemblies (furnace sintering, laser sintering, thermal spraying, consolidation of mechanical-milled composite metal (CNT powders), and so forth) [18, 19], there are fewer studies involving the obtainment of metal-carbon nanomaterial coatings [27]. These coatings can be obtained through several technologically relevant and upscalable approaches, among which cladding by preplacing a mixture of CNTs and metal powder on the metallic substrate in the form of a paste followed by selective melting with a concentrated energy source (continuous wave lasers, pulsed lasers, and focused electron beams) [1, 12, 15, 16, 20] or thermal spraying of metal-CNT powder mixtures [28] is the most employed. Most studies about laser-cladded metal-CNT coatings have been conducted on nonferrous metal powders and substrates (mainly based on copper, aluminium, and titanium) [27, 29]. Comparatively, nickel and iron-based coatings reinforced with CNTs, in conjunction with steel substrates, bearing a higher application potential than nonferrous coatings, have attracted considerably less attention, due to their relatively high susceptibility to embrittling and cracking [2, 21].

Therefore, the aims and elements of novelty of this study are to demonstrate the feasibility of the pulsed laser cladding method to obtain nickel-based hardcoatings on a mild steel substrate, starting from a preplaced commercial NiCrBSiFeC powder, mechanically blended with single-walled carbon nanotubes (SWCNTs), and to assess the effects of nanotube addition on the morphology, microstructure, hardness, hard phase composition, tribological properties, and corrosion resistance of the obtained assembly. Up to date, there are no articles that have used this type of feedstock powder (metallic combined with nanotubes) in conjunction with laser cladding for the obtainment of hardcoatings. Since the best processing speeds and quality of hardcoatings are achieved when the laser energy is efficiently absorbed by the feedstock material, using pulsed lasers instead of continuous wave ones could increase the throughput of the process, contribute to a lower heat-affected zone, and maximize the "chemical" embedding of the SWCNTs into the metallic matrix, since the pulsed lasers can deliver shorter

energy pulses each with a higher peak power than continuous wave lasers.

2. Materials and Methods

The commercial Metco 12C powder used for the cladding test (Sulzer Metco 12C) was purchased from Sulzer Metco Inc., with the following elemental composition (wt. %, according to producer specifications): 84.5% Ni, 7.5% Cr, 1.7% B, 3.5% Si, 2.5% Fe, 0.25% C, and the balance representing the Ni base. The SWCNTs have been purchased from Sigma-Aldrich and were of >85% purity and average diameter distributions between 1.3 and 2.3 nm and median length > 5 μm.

AISI 5140 (EN 10083-1, grade 37Cr4) steel has been used as a substrate for coating deposition. Workpieces with a dimension of $60 \times 25 \times 8$ mm have been fabricated by milling from the same raw material in order to prevent any structural or morphological variation between the samples. Before coating, the substrate surface was polished to a 0.8 μm grit and washed several times with ethanol (98% wt.), to remove the trace of organic contaminants.

The NiCrBSiFeC powder and SWCNTs (0.2% weight SWCNTs reported to the metallic powder) were mechanically blended by using a FRITSCH Planetary Micro Mill PULVERISETTE 7 with hardened stainless steel grinding spheres. The optimum metal powder/SWCNT weight ratio reported in this paper has been chosen based on preliminary studies which indicated high susceptibility to cracking for the composite coating with higher SWCNT loadings. The milling time was 40 minutes at 450 rpm speed, ensuring optimal embedding of the SWCNTs into the metal phase, based on prior experimenting of milling time optimization. The temperature of the grinding bowls was kept below 70°C to prevent any morphological changes of the powder.

In Figure 1 is presented the powder morphology after the mixing process with CNTs. The spherical shape of the powder is maintained after the rotational ball milling, and only minor deformation can be observed due to the impact with the steel balls. The SEM analyses emphasize a good adherence of the CNTs to the particle of NiCrBSiFeC (Figure 1).

The mechanically blended powder was mixed with a 12% wt. poly(vinyl alcohol) (PVA) (purchased from Sigma-Aldrich, the average polymerization degree of 900 and a hydrolysis degree of 98.5%) aqueous solution until the obtainment of a homogenous and free-flowing viscous paste. The paste has been preplaced on the steel substrates and kept at room temperature for 4 hours until complete water evaporation, ensuring a final thickness of 2 mm for the mixture.

A Nd:YAG ROFIN TRUPULSE 556 laser system ($\lambda_{max} = 1064$ nm) and a Precitec YC50 cladding module manipulated by a 6-axes CLOOS robot have been used for the laser cladding experiments. Argon of 99% purity at an 18 l/min flow rate was used as shielding gas for the preplaced powder. The cladded layer was fabricated by laser cladding of 12 partially overlapped tracks on the base material with the following parameters: 1500 W laser power, 1.3 mm spot diameter, 3 J laser energy, pulse duration 2 ms, 90 Hz frequency, and deposition speed: 27 cm·min^{-1}, as summarised
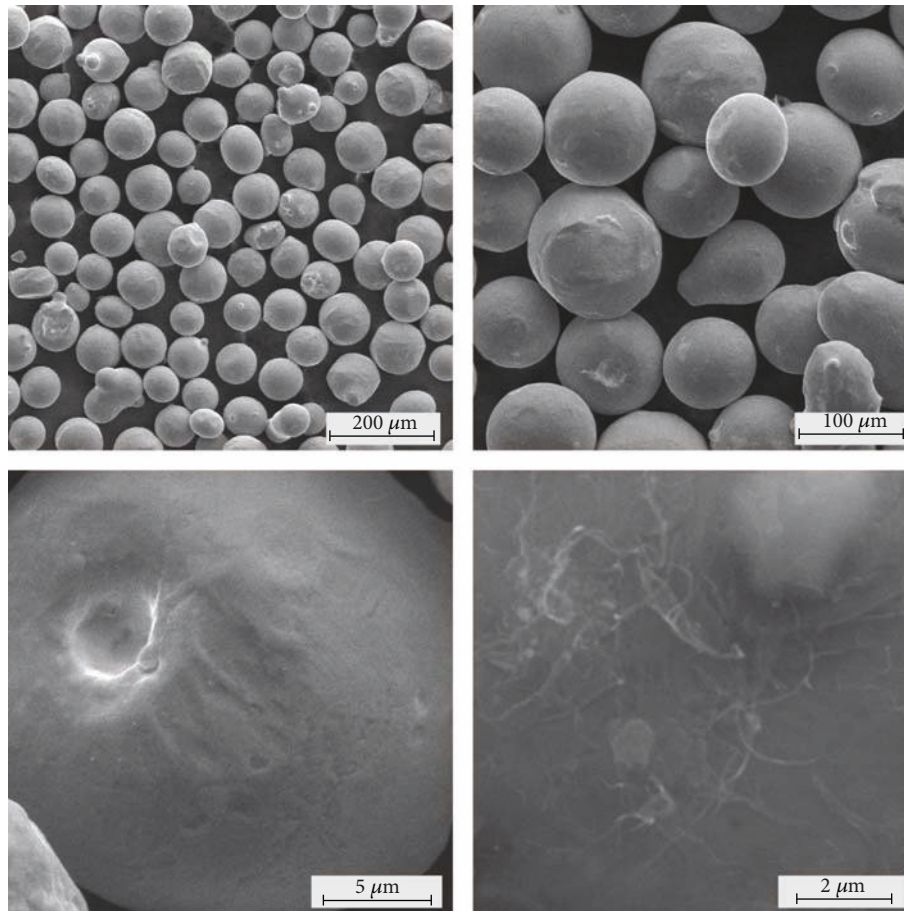
FIGURE 1: SEM micrographs at different magnifications of NiCrBSiFeC powder milled with SWCNT.

in Table 1. The overlapping degree was 45%. The schematic representation of the laser cladding procedure is presented in Figure 2.

Three sample batches of samples 1 and 2 have been obtained following the procedure as mentioned above, to ensure the repeatability of the results. The reference sample (sample 1), without SWCNTs in the composition, has been obtained following the same procedure.

The microstructure of the cladded specimens has been studied both on the surface of the coating (the surface was levelled, the top 1/3 of the coating being removed) and in cross-section. The samples (on both surfaces and cross-section) were ground, polished to $0.5\,\mu$m, and finally etched for 5 s with $3:1$ (vol : vol) $HCl:HNO_3$ reagent (aqua regia). A Leica DM ILM inverted microscope (50x, 200x, and 500x) and a VegaTescan LMHII scanning electron microscope (SEM) were used to acquire the micrographs of the cladded assemblies.

The hardness testing of the coatings has been performed ex situ using a MICROMET-5124VD Buehler microdurometer with loads from 0,5 gf up to 2000 gf. The setup test was 0.5 gf and 10 sec. dwell time, and the medium value of three indentations was used as a nominal value.

The wearing behaviour of the cladded samples was investigated using a commercial rotation tribometer from CSM Instruments using the ball on disk method with a steel ball with 6 mm diameter. The wear test was carried out at room temperature (temperature: 24°C, humidity: 32 (%)) without lubricant on 100 (m) using a normal load of 5 (N) and a linear speed of 5 (cm/s).

The crystallinity of the cladded layers was investigated using a Bruker D8 Discover X-ray Diffractometer (CuKα1 = 1.5406 A, locked-coupled technique, step size 0.02, scan speed 3 s/step, and 2θ range from 20 to 80°).

The corrosion resistance of the cladded layer has been tested using a conventional potentiostat/galvanostat setup and EC LAB software. The coated samples were used as the working electrodes, platinum as the counter electrode, and a saturated calomel $Hg|Hg_2Cl_2$ electrode as reference. The electrolyte employed was an aqueous 9% wt. NaCl solution. The tested surface used as the working electrode was 10×10 mm. The specimens were equilibrated for 30 min in the NaCl aqueous solution for obtaining a steady open circuit potential.

3. Results and Discussions

After the laser cladding process, the samples have been analysed in cross-section and on the top surface that was previously machined.

The coating-substrate interface is characterised by a good bonding and a geometrical dilution (η) of 20 and 25% between the cladded layer and the substrate. The base

TABLE 1: Parameters of the laser cladding process.

Powder	Sample	Laser power (W)	Laser energy (J)	Parameters Pulse (ms)	Frequency (Hz)	Speed (cm/min)
NiCrBSiFeC	Sample 1 *Reference (without CNTs)*	1500	3	2	90	27
	Sample 2 *With CNTs*	1500	3	2	90	27
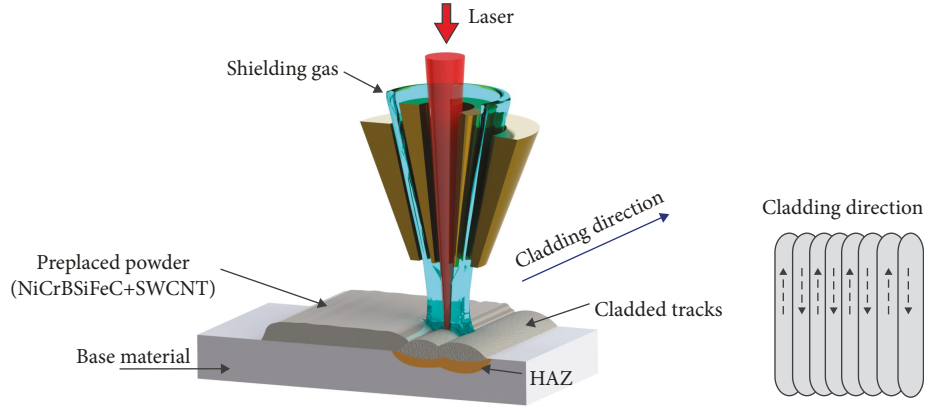
FIGURE 2: Principle of preplaced laser cladding of NiCrBSiFeC/CNT powder.

material presents a ferito-pearlitic structure with lamellar pearlite that was transformed during laser processing into a martensite or austenite structure in the heat-affected zone.

3.1. Morphology and Microstructure. Figure 3 shows the cross-sections for the reference sample and the CNT-fabricated sample with the addition of carbon nanotubes. The only difference between the samples, meaning compositional and laser processing, is the addition of single-walled carbon nanotubes in the composition of sample 2. In both cases, the cladded layer is free of cracks and pores and has a typical structure, common to both powder metallurgy and laser cladding processes (Figures 3(a) and 3(b)).

The bottom part of the coating contains a typical powder metallurgy feature, which resulted from the coalescence of the uniformly melted metal particles, namely, a 5 μm thick planar crystal, as represented also in the principle mechanism form (Figure 4). Due to the verticality of the heat gradient and to the high cooling ratios, the individual melt pools above the planar base crystal tend to crystalize in long primary dendrites (Figures 3(c) and 3(d)). The subsequent passing of the laser beam in adjacent regions determines the remelting of the tops of the dendrites, with the formation of equiaxed crystals, which can be found near the top of the coating (Figures 3(e) and 3(f) and the principle mechanism scheme from Figure 4).

To quantitatively assess the microstructural grain refinement that the CNTs promote in the coating, the ImageJ software (with the *Analyze Particles* plugin) was used to automatically compute the grain boundaries from the selected optical micrographs (i.e., Figures 3(e) and 3(f)) and plot the histogram of grain area frequency, following the contrast enhancement and binarization of the images.

CNT addition determines a more uniform distribution of grain dimensions and a higher proportion of equiaxed crystals, as it can be seen from Figure 3(g), probably due to its confining effect on the melted metal particle (being concentrated in the walls of the initial spherical metal particles that expand during melting), and subsequently, presenting high thermal conductivities, it could act as local heat gradient disruptors, leading to the preferential formation of uniform crystals, rather than dendrites, as is the case with the reference powder.

Due to the localised microstrains occurring in adjacent melt pool boundaries, the dendrite growth does not occur entirely in the direction of the heat gradient. In this respect, misalignments could be observed, as illustrated in Figure 5, for both reference and sample fabricated with CNTs. Higher misalignments could be observed in the case of the sample fabricated with CNTs, probably due to the local disruption in the heat gradient and due to grain growth hindrance.

Similar microstructural patterns can be found on the machine-levelled surface of the coatings. In Figure 6 is presented the microstructural appearance after the 1/3 from the top of the coatings was removed showing the dendrite structures which are sectioned in their growth direction.

Very long dendrite arms are observed in the region of the track overlapping area (Figure 7) and a more uniform structure in the middle of each cladded track. Therefore, it can be assumed that a high growth rate of the dendrite structure is increased during the remelting that occurred during the partial overlapping of the tracks.

Figure 7 reveals the differences of the grown pattern of the columnar dendrite with and without the addition of CNTs. The CNT additives determine the refining of the grain microstructure and homogeneity. As indicated in

(a)

(b)

(c)

(d)

(e)

(f)

(g)
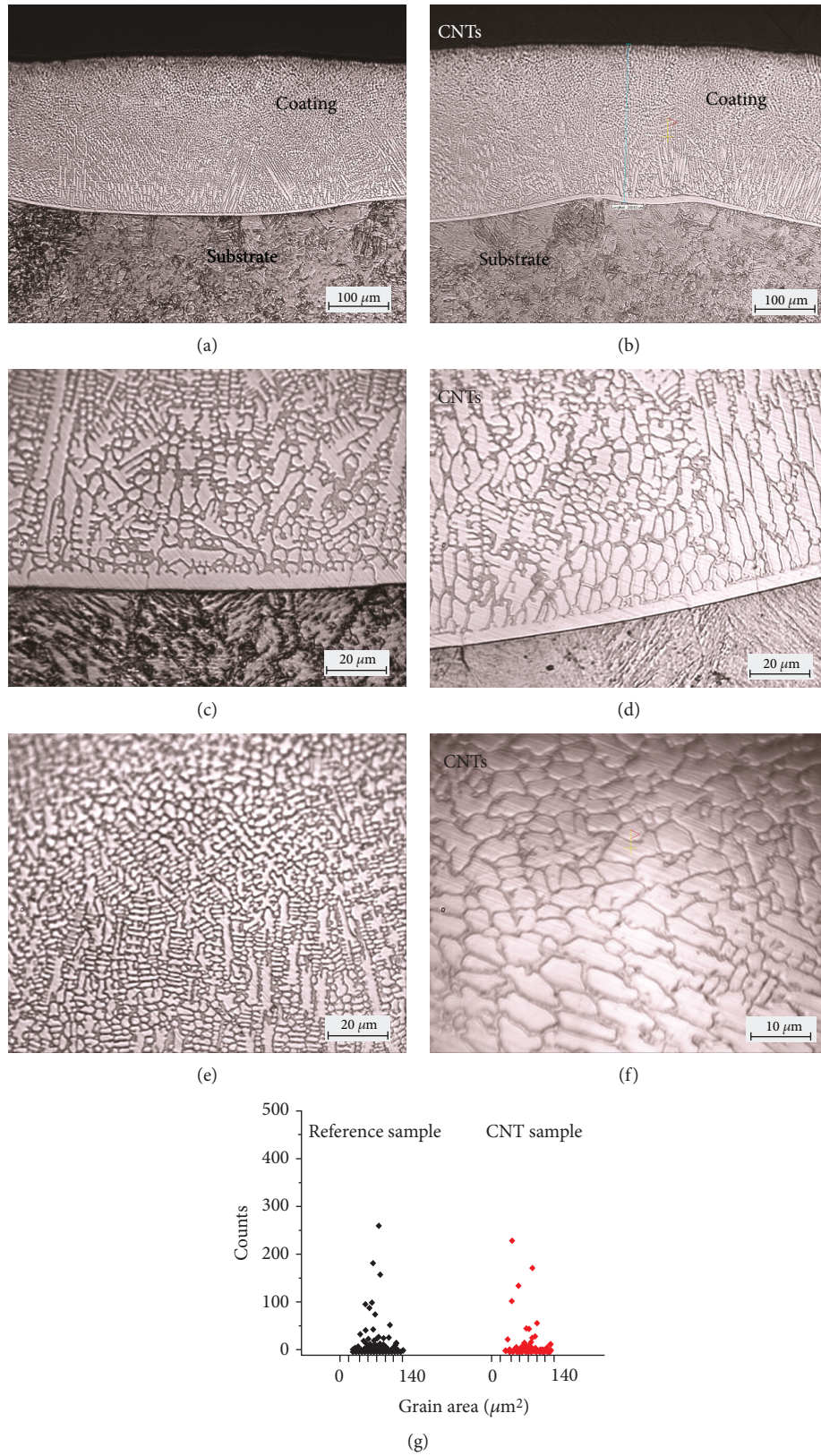
FIGURE 3: Cross-section microscopy of the cladded layer of reference sample 1 (a, c, e) and of sample 2 with CNT addition (b, d, f); (g) show the grain area distribution histograms.
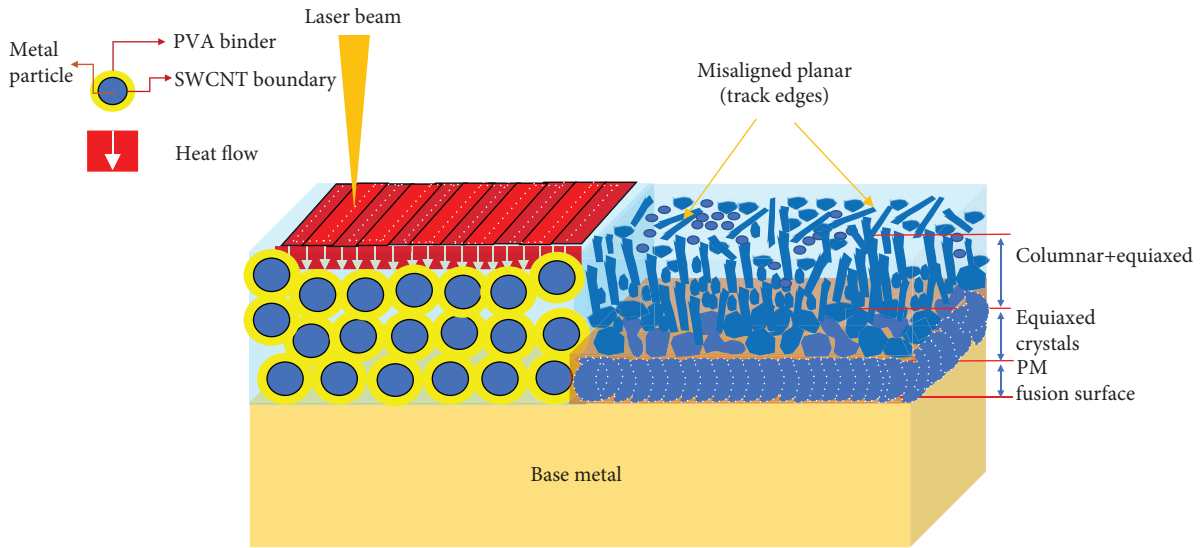
FIGURE 4: Schematic representation of the growth mechanism of a dendrite structure.
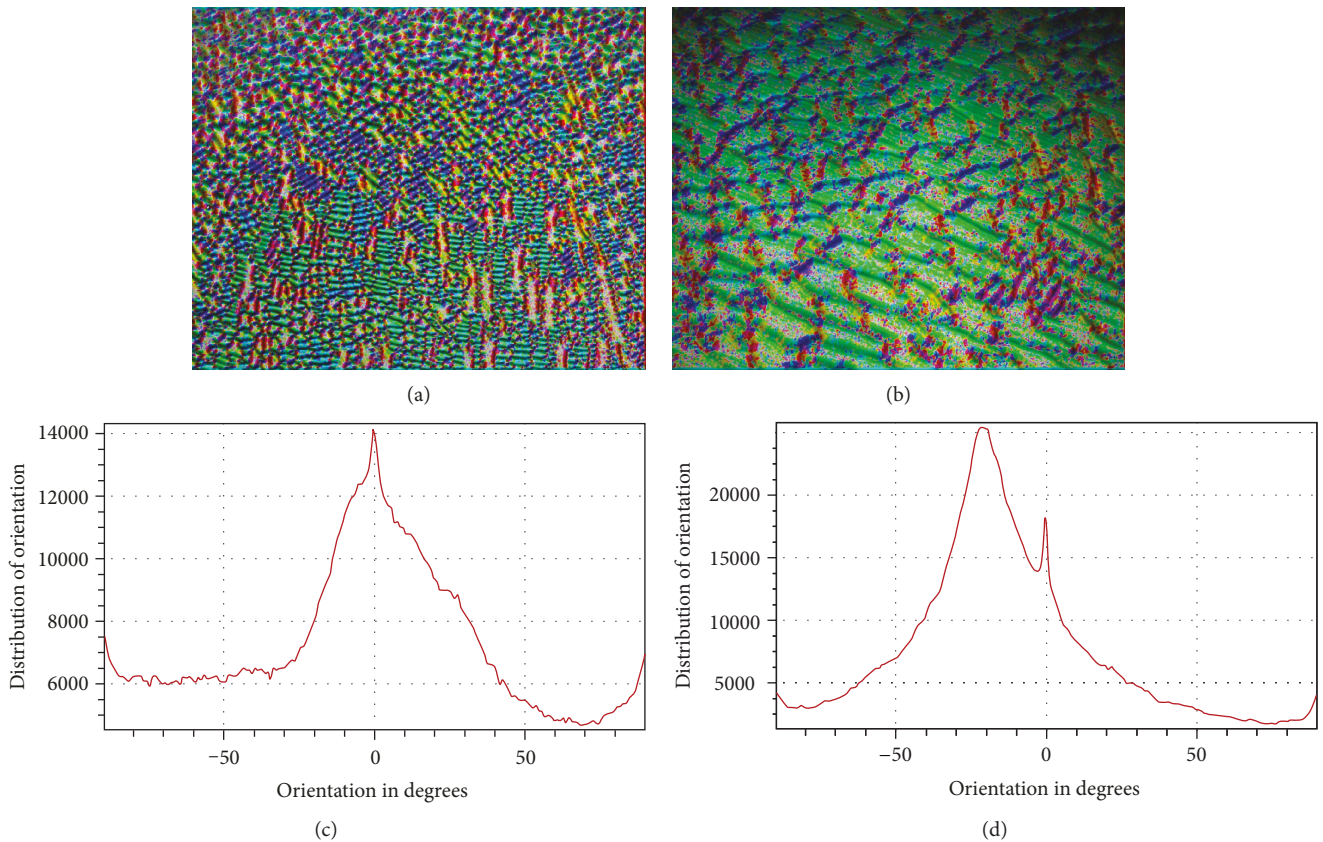
FIGURE 5: Grain orientation angle mapping and plot (obtained by ImageJ software—OrientationJ plugin).

Figure 7, sample 1 has a large variety of dendrite shapes from equiaxed to elongated with dimensions between 2 μm and 400 μm.

The grain dimension is smaller in the case of the cladded layer obtained with the nanotube addition as shown in Figures 7(b) and 7(d). The CNT addition influences the growth of mainly equiaxed dendrite. The high thermal con-

ductivity of the CNTs determines a nonpreferential growth direction of the dendrites while in the case of the reference sample, the crystallization is orientated along the heat flow produced during the laser processing.

The SEM overall appearance of the dendrite structure agrees with the optical microscopy presented in Figure 8. The grains are well fused into the matrix without any defects
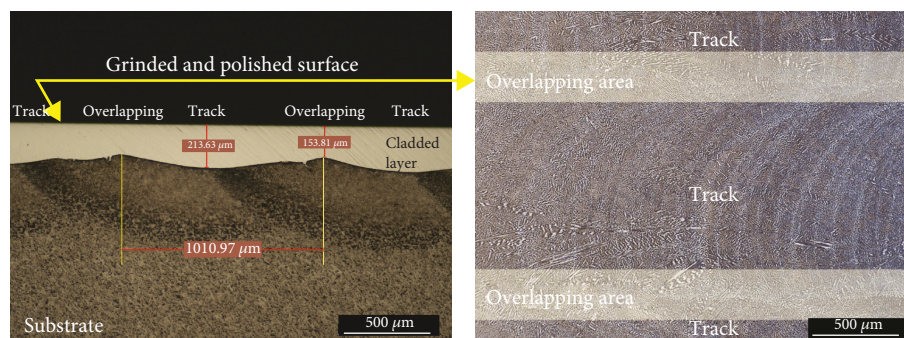
FIGURE 6: Top surface profile of the reference sample after 1/3 was removed.
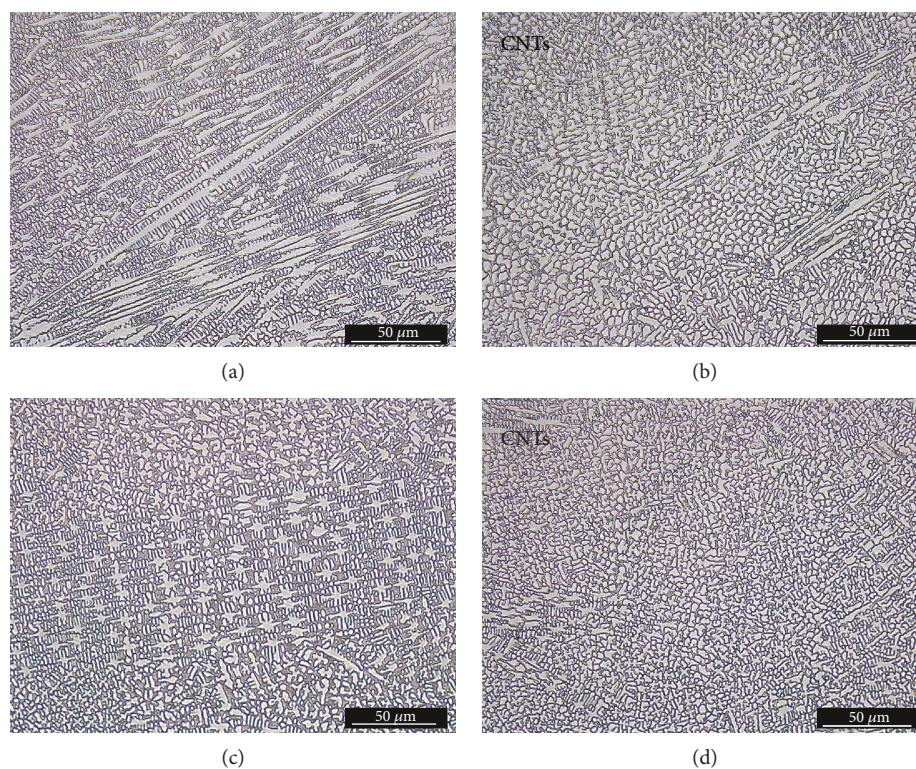
FIGURE 7: Microstructure of the machined top surface: (a, c) reference sample and (b, d) CNT composite coating.

such us pores, inclusions, or microcracks. The nanotubes could be included at the grain boundaries (the lighter colours indicate the higher rigidity/hardness of the structure).

The CNTs that have not been decomposed during the laser cladding process can be found as interstitial solid solution with the nickel and iron and possible monodispersed hard phases with chromium and boron. The hard phases (with the possible remainder of carbon nanotubes) are segregated at the grain boundaries which is in accordance with the AFM images from Figure 9. The AFM cantilever is influenced by the Young elastic modulus of the material (i.e., hardness, rigidity). Therefore, the soft and hard phases of the material can be distinguished by using the cantilever vibration movement. In Figure 9, lighter colour indicates the areas with a higher hardness-rigidity domain (e.g., carbides and intermetallic compounds) and darker colour indicates the surfaces with lower hardness.

The crystalline structure of both samples was analysed by XRD Figure 10. The diffractograms indicate that the cladded layer is composed of a complex mixture of borides and carbides ($Cr_{23}C_6$, Cr_7C_3, and Ni_4B_3) arranged in an iron nickel (FeNi) matrix.

It can be observed that the main phases identified, namely, FeNi, $Cr_{23}C_6$, Cr_7C_3, Ni_4B_3, and C, are similar for both samples. The main difference between the samples is observed at 44.58° where a high intensity peak identified as Cr_7C_3 appears in the case of CNT composite coating.

3.2. Microhardness Characteristics of Composite Coatings.

The coatings fabricated with the Metco 12C powder (NiCrB-SiFeC) are characterised by a low hardness (370 HV03) with the benefits of a very low cracking susceptibility and a good machinability. The testing shows that composite coatings have a 364 HV03 microhardness compared with the

(a)

(b)

(c)

(d)
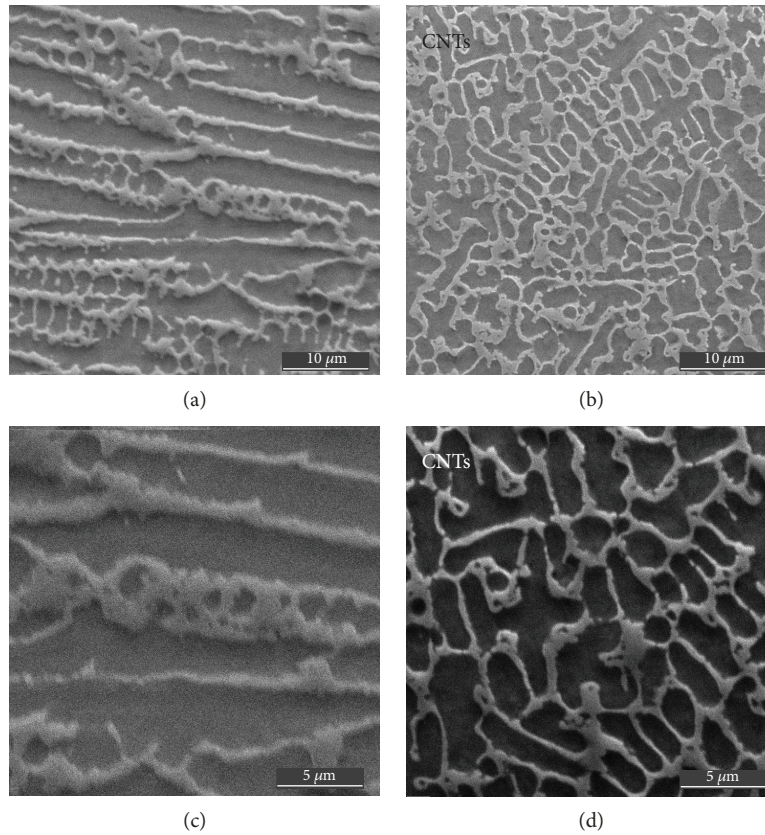
FIGURE 8: SEM microscopy of the machined top surface: (a, c) reference sample and (b, d) CNT composite coating.
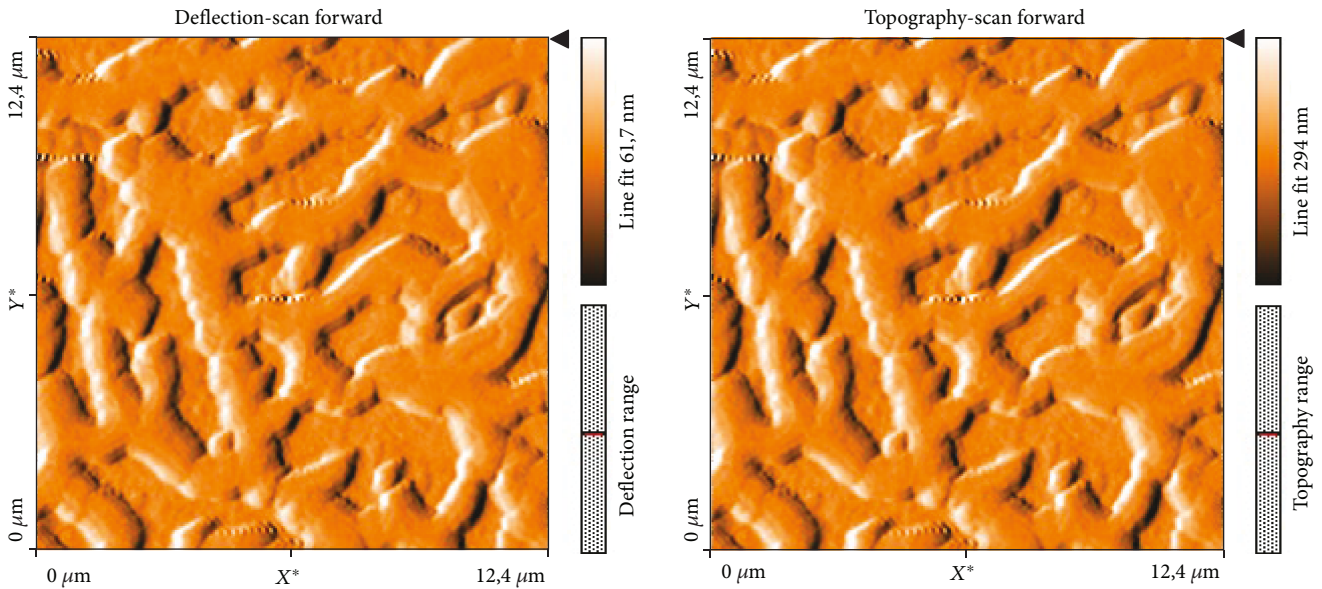
FIGURE 9: Atomic force microscopy on the composite sample using deflection and topography scanning mode.

reference sample characterised by a microhardness value of 342 HV03. The microhardness testing on the sample cross-section shows a decrease from the top of the coatings to the bottom of the coating due to the iron diffusion from the base material.

The microhardness testing on specific dendrite and interdendrite structures is a useful tool to compare the microhardness of the coating with and without the addition of CNTs. Due to the low loading (0.5 gf), the indentations can be located exactly on the interface line with the substrate and on the dendrite arms. Figure 11 shows the results obtained on the reference sample being obvious that interdendrite areas (Ni matrix) have almost double microhardness compared with the dendrite arms.

FeNi △

Fe$_{0.612}$Ni$_{0.388}$ ◇

(Fe$_3$Ni$_2$)$_{0.4}$ ▲

Cr$_{23}$C$_6$ □

Cr$_7$C$_3$ ■

Ni$_4$B$_3$ ⋈

C carbon ☆
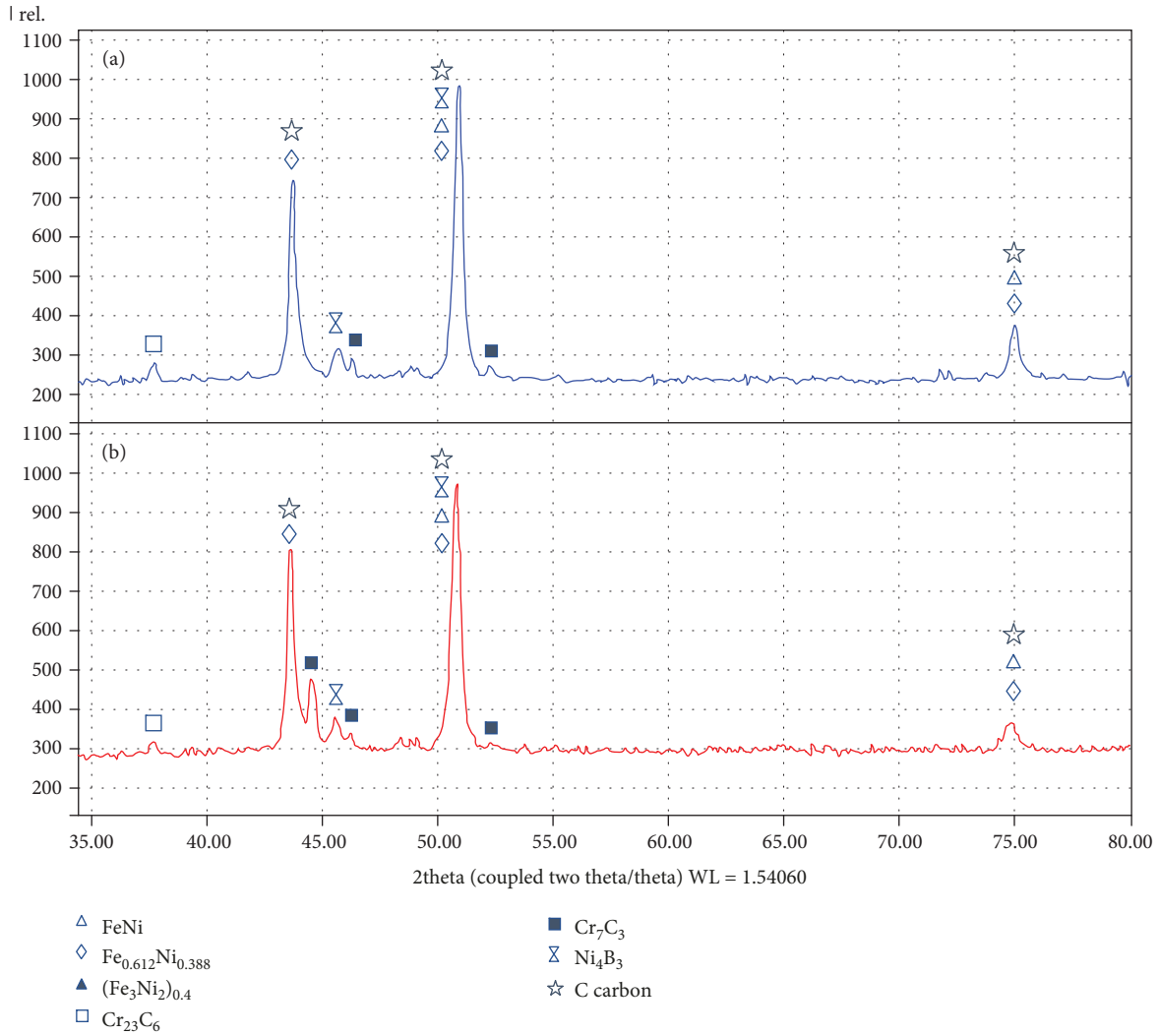
FIGURE 10: XRD diffractogram of the reference sample (a) and CNT composite coating (b).
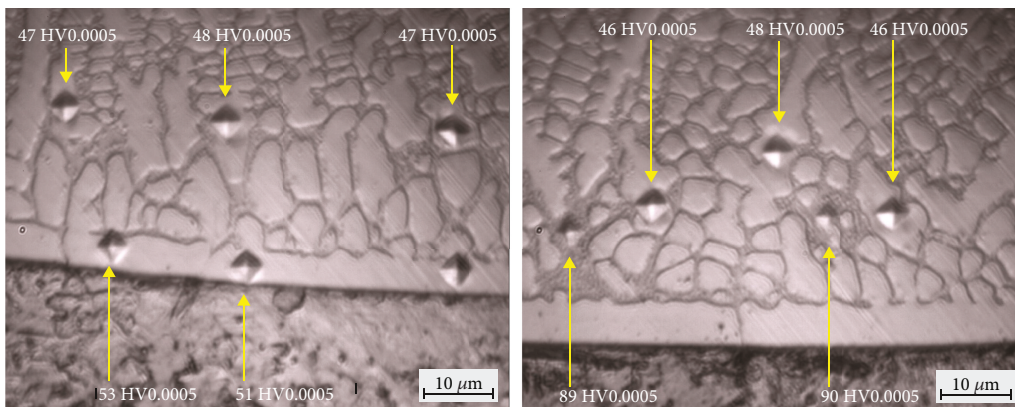
FIGURE 11: Microindentation on the dendrite arm and on the interdendrite area of the cross-section of sample 1, loads 0.0005 kgf.

Addition of CNTs has no major influence near the interface with the substrate, where a microhardness between 50 HV0.0005 and 59 HV0.0005 has been recorded mainly because in this zone the cooling rate is too high and the grain dimension is not reduced.

The microhardness improvement in the case of sample 2 occurs in the top part of the composite coatings (Figure 12(a)) where the microstructure refinement produces better intergranular adhesion and reduces the dislocation density. According to Figures 11 and 12, the microhardness

(a)

(b)

(c)
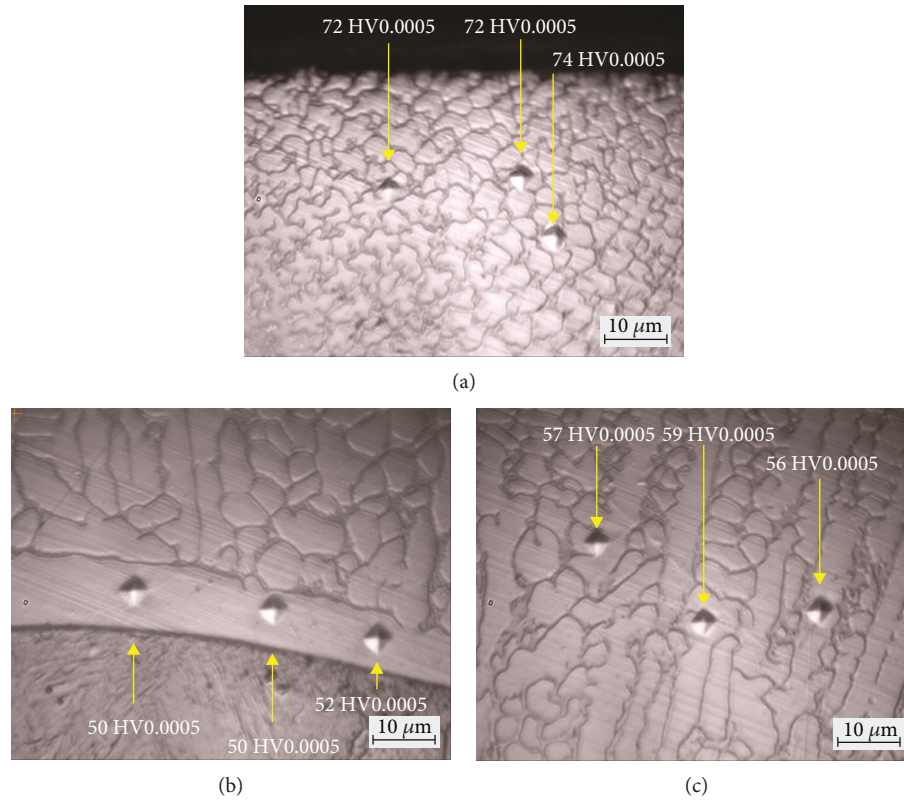
FIGURE 12: Microindentation on the white dendritic formation on the cross-section of sample 2, loads 0.0005 kgf.
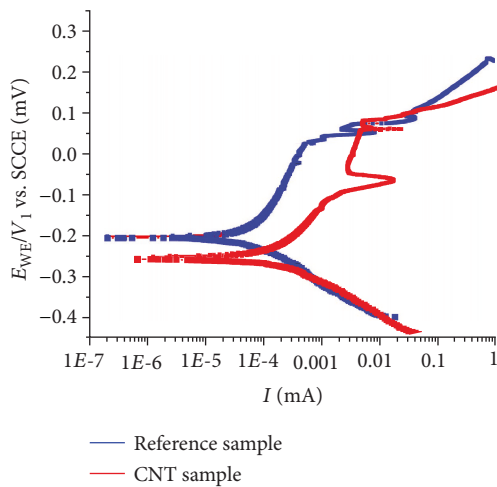
FIGURE 13: Polarization curves of the reference sample (sample 1) and of the CNT sample (sample 2).

TABLE 2: Corrosion test parameters and results.

Operational parameters	Sample 1 (reference)	Sample 2 (CNTs)
Ecorr	-207.373 mV	-256.253 mV
Icorr	0.073 μA	0.036 μA
Bc	99.1 mV	76.2 mV
Ba	271.2 mV	161.9 mV
Chi^2	3 872.35	134.92
Corrosion rate	0.228 134 e-3 mmpy	0.138 091 e-3 mmpy

index) and the corrosion rate decreases in the case of the CNT composite sample.

The potential of the CNTs is much higher than that of Ni compounds and chromium/boron hard phases resulting in improved corrosion resistance of the composite coating. Moreover, the addition of the CNTs into the Ni-based matrix determines the microstructure refinement which is beneficial in the case of corrosion resistance. An almost 40% lower corrosion rate compared with the reference sample is obtained by the addition of CNTs.

tested on the dendrite formation increases from 59 HV0.0005 to 74 HV0.0005 in the case of sample 2.

3.3. Corrosion Resistance of the Composite Coatings. The corrosion rate was measured through the intensity of the corrosion current and, respectively, the Tafel plots presented in Figure 13. It has been determined that sample 2 fabricated with the addition of CNTs has a better corrosion resistance than the reference sample (sample 1). As presented in Table 2, the value of corrosion current density (Icorr

3.4. Wear Properties of Composite Coatings. The ball on disk testing with similar conditions for both samples has been carried out to determine the wear behaviour of the composite coating. The test results show no significant differences between the two samples, noting only a slightly better wear resistance of the CNT composite coatings. Also, the coefficient of friction of the composite layer is 10% higher (sample

Wear rate: 1.531E−005 mm³/n/m

Wear rate: 1.452E−005 mm³/n/m
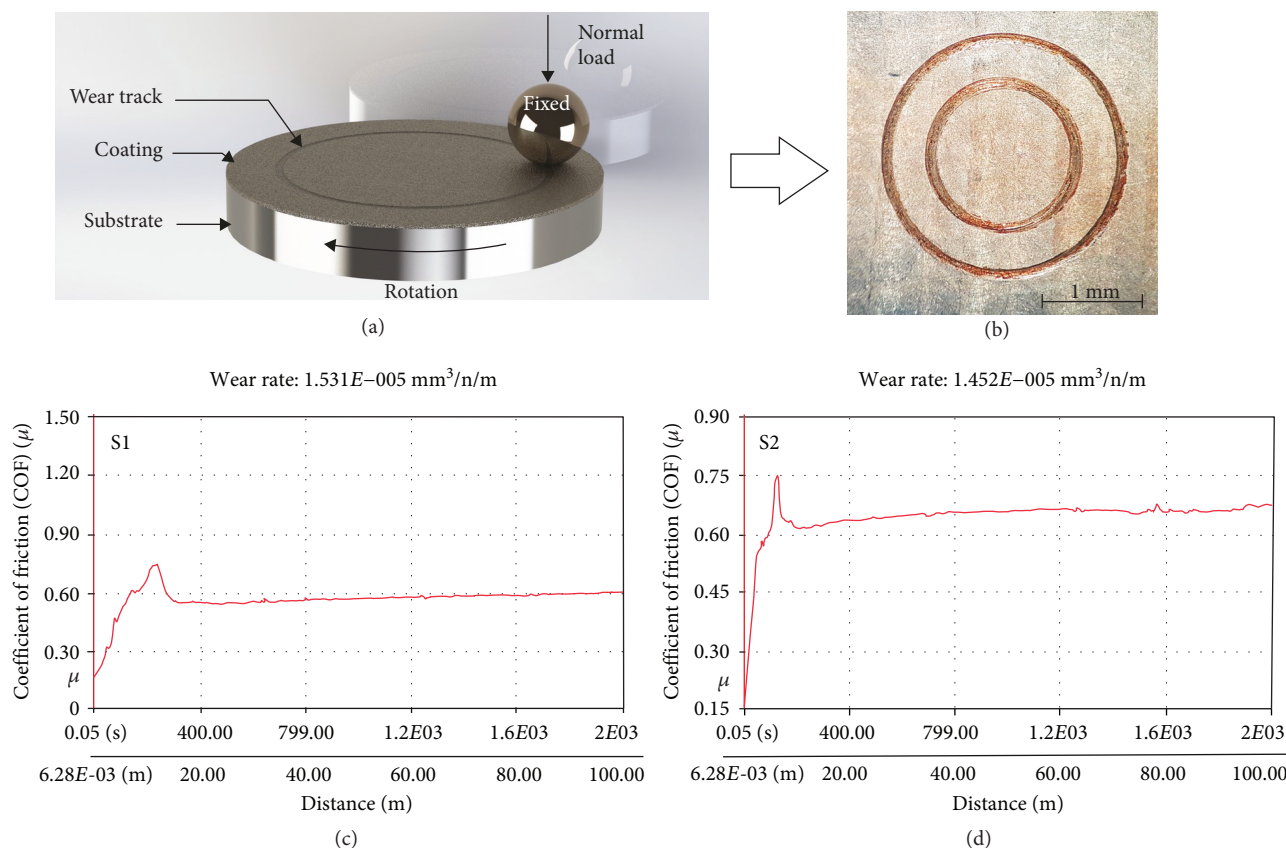
FIGURE 14: Wear results: (a) schematic representation of the ball on disk testing, (b) wear tracks on the surface of sample 1, and (c, d) plot of COF vs. distance of sample 1 and sample 2.

1: 0.59μ and sample 2: 0.66μ) compared with the reference sample (Figures 14(a) and 14(b)). It is well known that carbon nanotubes are a good lubricant material, but in this case, the CNT addition promotes the formation of hard phases (Cr_7C_3) with an increased hardness, as determined by the microhardness testing and the XRD diffractogram. Therefore, the higher coefficient of friction has no direct influence on the wear rate of the composite coatings.

4. Conclusions

An alternative approach for obtaining improved mechanical behaviour and corrosion resistance of nickel-based coatings was used by addition of single-walled carbon nanotubes. Crack-free coatings have been fabricated by the preplaced laser cladding method on a low carbon steel substrate.

The addition of CNTs determines different crystallization patterns in the laser-cladded coatings, with a more uniform distribution of grain shape and dimensions, through the local disruption in the thermal gradient direction and growth hindrance. The morphology of the coatings consists in misaligned dendrites, without second- and higher-order hierarchy, along with epitaxially grown crystals separated from the steel substrate by a 5μm thick planar crystal. The CNT addition refines the microstructure and promotes the formation of hard phases such as Cr_7C_3, resulting in improvement of the corrosion resistance with 40% and

microhardness with 25%, as well as the enhancement of the wear resistance with 5.5% in comparison with the reference sample realised without the addition of CNTs. Overall, even if the improvement percent is not impressive, it can be concluded that the obtained morphology has a positive influence on the microhardness, corrosion, and wear resistance of the assembly, leading to the obtainment of improved value-added materials at minimal carbon nanotube loadings.

Data Availability

All the experimental data used to support the findings of this study are included within the article. Any supplementary data regarding the present research could be supplied by the correspondent author upon request.

Conflicts of Interest

The authors declare that they have no conflicts of interest.

Acknowledgments

References

[1] M. Dhanda, B. Haldar, and P. Saha, "Development and characterization of hard and wear resistant MMC coating on Ti-6Al-4V substrate by laser cladding," *Procedia Materials Science*, vol. 6, pp. 1226–1232, 2014.

[2] D. Lin, C. Richard Liu, and G. J. Cheng, "Single-layer graphene oxide reinforced metal matrix composites by laser sintering: microstructure and mechanical property enhancement," *Acta Materialia*, vol. 80, pp. 183–193, 2014.

[3] L. A. Dobrzański, A. Grajcar, and W. Borek, "Microstructure evolution of high-manganese steel during the thermomechanical processing," *Archives of Materials Science*, vol. 70, p. 70, 2009.

[4] P. Olier, J. Malaplate, M. H. Mathon et al., "Chemical and microstructural evolution on ODS Fe–14CrWTi steel during manufacturing stages," *Journal of Nuclear Materials*, vol. 428, no. 1-3, pp. 40–46, 2012.

[5] H. Springer, R. Aparicio Fernandez, M. J. Duarte, A. Kostka, and D. Raabe, "Microstructure refinement for high modulus in-situ metal matrix composite steels via controlled solidification of the system Fe–TiB$_2$," *Acta Materialia*, vol. 96, pp. 47–56, 2015.

[6] S. Bao, G. Zhao, C. Yu, Q. Chang, C. Ye, and X. Mao, "Recrystallization behavior of a Nb-microalloyed steel during hot compression," *Applied Mathematical Modelling*, vol. 35, no. 7, pp. 3268–3275, 2011.

[7] R. Casati and M. Vedani, "Metal matrix composites reinforced by nano-particles—a review," *Metals*, vol. 4, no. 1, pp. 65–83, 2014.

[8] H. Dieringa, "Properties of magnesium alloys reinforced with nanoparticles and carbon nanotubes: a review," *Journal of Materials Science*, vol. 46, no. 2, pp. 289–306, 2011.

[9] J. P. Tu, Y. Z. Yang, L. Y. Wang, X. C. Ma, and X. B. Zhang, "Tribological properties of carbon-nanotube-reinforced copper composites," *Tribology Letters*, vol. 10, no. 4, pp. 225–228, 2001.

[10] R. S. Raveendra, P. V. Krupakara, P. A. Prashanth, and B. M. Nagabhushana, "Enhanced mechanical properties of Al-6061 metal matrix composites reinforced with α-Al$_2$O$_3$ nanoceramics," *Journal of Materials Science & Surface Engineering*, vol. 4, no. 7, pp. 483–487, 2016.

[11] K. M. Shorowordi, T. Laoui, A. S. M. A. Haseeb, J. P. Celis, and L. Froyen, "Microstructure and interface characteristics of B$_4$C, SiC and Al$_2$O$_3$ reinforced Al matrix composites: a comparative study," *Journal of Materials Processing Technology*, vol. 142, no. 3, pp. 738–743, 2003.

[12] Q. H. Li, M. M. Savalani, Q. M. Zhang, and L. Huo, "High temperature wear characteristics of TiC composite coatings formed by laser cladding with CNT additives," *Surface and Coatings Technology*, vol. 239, pp. 206–211, 2014.

[13] V. B. Niste, M. Ratoi, H. Tanaka, F. Xu, Y. Zhu, and J. Sugimura, "Self-lubricating Al-WS$_2$ composites for efficient and greener tribological parts," *Scientific Reports*, vol. 7, no. 1, article 14665, 2017.

[14] J. Y. Hwang, A. Neira, T. W. Scharf, J. Tiley, and R. Banerjee, "Laser-deposited carbon nanotube reinforced nickel matrix composites," *Scripta Materialia*, vol. 59, no. 5, pp. 487–490, 2008.

[15] M. M. Savalani, C. C. Ng, Q. H. Li, and H. C. Man, "In situ formation of titanium carbide using titanium and carbon-nanotube powders by laser cladding," *Applied Surface Science*, vol. 258, no. 7, pp. 3173–3177, 2012.

[16] M. J. Hamedi, M. J. Torkamany, and J. Sabbaghzadeh, "Effect of pulsed laser parameters on in-situ TiC synthesis in laser surface treatment," *Optics and Lasers in Engineering*, vol. 49, no. 4, pp. 557–563, 2011.

[17] A. Sanaty-Zadeh, "Comparison between current models for the strength of particulate-reinforced metal matrix nanocomposites with emphasis on consideration of Hall–Petch effect," *Materials Science and Engineering A*, vol. 531, pp. 112–118, 2012.

[18] S. R. Bakshi, D. Lahiri, and A. Agarwal, "Carbon nanotube reinforced metal matrix composites - a review," *International Materials Review*, vol. 55, no. 1, pp. 41–64, 2010.

[19] S. C. Tjong, "Recent progress in the development and properties of novel metal matrix nanocomposites reinforced with carbon nanotubes and graphene nanosheets," *Materials Science and Engineering: R: Reports*, vol. 74, no. 10, pp. 281–350, 2013.

[20] M. Iqbal, I. Shaukat, A. Mahmood, K. Abbas, and M. A. Haq, "Surface modification of mild steel with boron carbide reinforcement by electron beam melting," *Vacuum*, vol. 85, no. 1, pp. 45–47, 2010.

[21] D. Lin, C. Richard Liu, and G. J. Cheng, "Laser sintering of separated and uniformly distributed multiwall carbon nanotubes integrated iron nanocomposites," *Journal of Applied Physics*, vol. 115, no. 11, article 113513, 2014.

[22] H. Kwon, M. Takamichi, A. Kawasaki, and M. Leparoux, "Investigation of the interfacial phases formed between carbon nanotubes and aluminum in a bulk material," *Materials Chemistry and Physics*, vol. 138, no. 2-3, pp. 787–793, 2013.

[23] W. Zhou, S. Bang, H. Kurita, T. Miyazaki, Y. Fan, and A. Kawasaki, "Interface and interfacial reactions in multi-walled carbon nanotube-reinforced aluminum matrix composites," *Carbon*, vol. 96, pp. 919–928, 2016.

[24] K. Chu, C. c. Jia, L. k. Jiang, and W. s. Li, "Improvement of interface and mechanical properties in carbon nanotube reinforced Cu–Cr matrix composites," *Materials & Design*, vol. 45, pp. 407–411, 2013.

[25] S. M. Uddin, T. Mahmud, C. Wolf et al., "Effect of size and shape of metal particles to improve hardness and electrical properties of carbon nanotube reinforced copper and copper alloy composites," *Composites Science and Technology*, vol. 70, no. 16, pp. 2253–2257, 2010.

[26] L. Ci, Z. Ryu, N. Y. Jin-Phillipp, and M. Rühle, "Investigation of the interfacial reaction between multi-walled carbon nanotubes and aluminum," *Acta Materialia*, vol. 54, no. 20, pp. 5367–5375, 2006.

[27] W. X. Chen, J. P. Tu, L. Y. Wang, H. Y. Gan, Z. D. Xu, and X. B. Zhang, "Tribological application of carbon nanotubes in a metal-based composite coating and composites," *Carbon*, vol. 41, no. 2, pp. 215–222, 2003.

[28] D. Mohanty, S. Kar, S. Paul, and P. P. Bandyopadhyay, "Carbon nanotube reinforced HVOF sprayed WC-Co coating," *Materials & Design*, vol. 156, pp. 340–350, 2018.

[29] S. R. Bakshi, V. Singh, K. Balani, D. G. McCartney, S. Seal, and A. Agarwal, "Carbon nanotube reinforced aluminum composite coating via cold spraying," *Surface and Coatings Technology*, vol. 202, no. 21, pp. 5162–5169, 2008.